

Article

Burned Area Classification Based on Extreme Learning Machine and Sentinel-2 Images

John Gajardo ^{1,†} , Marco Mora ^{2,*,†} , Guillermo Valdés-Nicolao ^{2,†} and Marcos Carrasco-Benavides ^{3,†} 

¹ Facultad de Ciencias Forestales y Recursos Naturales, Universidad Austral de Chile, Valdivia 5090000, Chile; john.gajardo@uach.cl

² Laboratorio de Investigaciones Tecnológicas en Reconocimiento de Patrones, Universidad Católica del Maule, Talca 3480112, Chile; gvaldez@ucm.cl

³ Departamento de Ciencias Agrarias, Universidad Católica del Maule, Curico 3340000, Chile; mcarrascob@ucm.cl

* Correspondence: mmora@ucm.cl

† These authors contributed equally to this work.

Abstract: Sentinel-2 satellite images allow high separability for mapping burned and unburned areas. This problem has been extensively addressed using machine-learning algorithms. However, these need a suitable dataset and entail considerable training time. Recently, extreme learning machines (ELM) have presented high precision in classification and regression problems but with low computational cost. This paper proposes evaluating ELM to map burned areas and compare them with other machine-learning algorithms broadly used. Several indices, metrics and training times were used to assess the performance of the algorithms. Considering the average of datasets, the best performance was obtained by random forest (DICE = 0.93; omission and commission = 0.08) and ELM (DICE = 0.90; omission and commission = 0.07). The training time for the best model was from ELM (1.45 s) and logistic regression (1.85 s). According to results, ELM was the best burned-area classification algorithm, considering precision and training time, evidencing great potential to map burned areas at global scales with medium-high spatial resolution images. This information is essential to fire-risk systems and burned-area records used to design prevention and fire-combat strategies, and it provides valuable knowledge on the effect of fires on the landscape and atmosphere.

Keywords: remote sensing; burned area classification; extreme learning machine; sentinel-2 images



Citation: Gajardo, J.; Mora, M.; Valdés-Nicolao, G.; Carrasco-Benavides, M. Burned Area Classification Based on Extreme Learning Machine and Sentinel-2 Images. *Appl. Sci.* **2022**, *12*, 9. <https://doi.org/10.3390/app12010009>

Academic Editor: Hyung-Sup Jung

Received: 8 November 2021

Accepted: 16 December 2021

Published: 21 December 2021

Publisher's Note: MDPI stays neutral with regard to jurisdictional claims in published maps and institutional affiliations.



Copyright: © 2021 by the authors. Licensee MDPI, Basel, Switzerland. This article is an open access article distributed under the terms and conditions of the Creative Commons Attribution (CC BY) license (<https://creativecommons.org/licenses/by/4.0/>).

1. Introduction

Wildfires are global phenomena that cause environmental and social transformations, including biodiversity loss, soil degradation, harm to human beings and economic losses [1]. Nowadays, there is growing concern over this matter since, under current climate change conditions, there will be an increase in the season duration, magnitude and consequences of wildfires [2]. In this context, it is increasingly necessary to have precise and detailed information regarding the affected area in order to both assess and consider damages and to implement prevention plans and processes of recovery of the infrastructure and ecosystems affected [3].

Satellite images provided by optical sensors can be used to delimit burned areas resulting from wildfires. This is possible due to the strong decrease of reflectance in the near-infrared (NIR) and the increase in the shortwave infrared spectrum (SWIR) of vegetation as a result of dryness caused by fire [4]. In addition, the difference in the information provided by satellite data can be used to estimate spectral indices, which help to describe the vegetation condition, the severity of the damage or the levels of carbonation of the areas affected by fires. The most common indices are burned-area index (BAI), normalized burn ratio (NBR) and normalized difference vegetation index (NDVI) [5].

In general terms, there are two approaches for the mapping of burned areas using satellite data. The first one is based on rules that identify variations in the burned spectral signals with respect to the unburned environment, based on which fixed or dynamic thresholds are defined for the spectral bands or indices [6]. The second approach is based on machine-learning algorithms that can learn the spectral features of a sample of pixels with labels and recognize those patterns in other areas of the image [7]. Machine-learning (ML) algorithms build a non-linear transformation whose parameters are estimated in a supervised or unsupervised way to solve classification, regression and clustering problems by formulating an optimization problem [8]. Recently, these types of algorithms have been used for mapping burned areas, showing good results with random forest (RF) [7,9], support vector machine (SVM) [7,10], logistic regression (LR) [11] and multilayer perceptron (MLP) supervised learning Neural Networks [7,12].

Despite the advances in the methodologies and algorithms employed, the estimation of burned areas using satellite images depends heavily on the spatial resolution of the sensor used. This demonstrates the significant underestimation of the calculations performed with low-resolution sensors when compared to estimations of higher resolution [13]. Therefore, it is deemed necessary to explore the use of higher spatial resolution platforms and sensors, such as Sentinel-2, in order to deal with these problems.

Moreover, most of the machine-learning algorithms that are frequently employed in image classification increase their computational cost when the size of the data sets increases, leading to longer training and classification times [14]. However, extreme learning machines (ELM) have recently attracted increasing interest in image classification due to their high accuracy levels, which are comparable to the traditional SVM and MLP, but with a training algorithm with reduced computational cost [15].

Considering the ELM algorithm training efficiency and its good generalization, we hypothesized that ELM neural networks can be used to classify burned areas on medium-spatial resolution images, showing a great potential to deal with this problem at scales that require a massive volume of data. Consequently, this work aims to propose the evaluation of mapping burned areas on Sentinel-2 images through an ELM neural network supervised classification, comparing ELM performance in terms of accuracy and training time to several machine-learning algorithms.

The rest of the article is organized as follows: Section 2 presents the methods used to evaluate the ELM performance with other algorithms. Section 3 presents the methodology of the experiments. Section 4 shows the results and their discussion. Finally, Section 5 presents the conclusions.

2. Fundamentals of the Classification Algorithms Applied

In this research, several classification algorithms were used, whose fundamentals are described below.

2.1. Extreme Learning Machine

Extreme learning machine (ELM) neural networks are known for their extremely fast learning speed, showing high levels of performance, compared to the ones found for multilayer perceptron network (MPL) and support vector machine (SVM) [16]. ELM has shown better performance than neural networks with backpropagation and other classification models, in terms of computational efficiency and proper generalization when applied to Landsat satellite images [17].

The ELM algorithm was originally developed for single-hidden layer feedforward neural networks. One of its main features is its simple training since the weights and biases of the hidden layer are randomly created and the output weights can be determined by the resolution of an overdetermined linear system by the use of the Moore–Penrose generalized inverse [16]. The output expression of a single-hidden layer ELM network is as follows:

$$f_L(x) = \sum_{i=1}^L \beta_i g(w_i * x_1 + b_1), j = 1, \dots, N \quad (1)$$

where:

L : the number of hidden neurons.

N : the number of training samples.

β_i : output layer's weight vector.

w : hidden layer's weight vector.

g : activation function.

b : biases parameters vector.

x : input vector.

Equation (1) can be written in the matricial form:

$$T = H\beta \quad (2)$$

where H is the hidden layer output matrix and β is the weight vector of the output layer. Specifically, the H matrix has the following structure:

$$H = \begin{bmatrix} g(w_1 * x_1 + b_1) & \dots & g(w_L * x_1 + b_L) \\ \vdots & \dots & \vdots \\ g(w_1 * x_N + b_1) & \dots & g(w_L * x_N + b_L) \end{bmatrix}_{N \times L} \quad (3)$$

where:

m : the number of outputs.

H : the hidden layer output matrix of the neural network.

T : the training data labels matrix.

Unlike gradient descent-based neural networks, for ELM, weights of the hidden layer need not be fitted since they are randomly created. In order to train an ELM network, it is necessary to find a $\hat{\beta}$ least-squares solution of the $H\beta = T$ linear system, whose expression is as follows:

$$\hat{\beta} = H^\dagger T \quad (4)$$

where H^\dagger is the Moore–Penrose generalized inverse of matrix H .

Given a $\aleph = \{(x_i, t_i) | x_i \in \mathbb{R}^n, t_i \in \mathbb{R}^L, i = 1, \dots, N\}$ training set, $g(x)$ activation function, and L number of hidden neurons, the ELM training algorithm has the following steps:

- **Step 1:** assign arbitrary input weight w_i and bias $b_i, i = 1, \dots, L$.
- **Step 2:** calculate the hidden layer output matrix H .
- **Step 3:** calculate the output weight β for $\beta = H^\dagger T$.

2.2. Multilayer Perceptron

Multilayer perceptron neural networks (MLP) are widely used for satellite images classification [18] and for burned area mapping applications [19]. These networks have an input layer, one or more hidden layers and an output layer [20]. They are fitted using the back-propagation algorithm, which consists of minimizing the output mean squared error of the network using a gradient descent algorithm [19,21]. In general, MLPs have poor performance when the optimization algorithm falls into local minimum and due to the overfitting phenomenon [18]. However, it is possible to improve the optimization algorithm performance through heuristic search techniques [21].

2.3. Random Forest

It is an ensemble model of several decision trees randomly organized and individually trained. Each tree makes a classification decision where the class with the maximum number of votes is determined for the input data [8]. Each tree is independently organized

so successive trees are independent from the previous ones [18]. Random forest (RF) has shown good performance in linear and nonlinear models known for balancing bias and variance [7]. This algorithm is widely used on satellite images data due to the high accuracy of its classifications [22]. One of its outstanding features is that it can successfully handle high data dimensionality and multicollinearity since both are insensitive to overfitting [23] and training algorithm is fast [24]. Moreover, RF has high accuracy for datasets external to those considered during training, which shows that spatial autocorrelation has a low impact on the prediction performance [25].

2.4. Logistic Regression

Logistic regression (LR) is a statistical model that can be used to describe the relationship between a dichotomous dependent variable and a series of independent variables [11]. LR has the function of predicting the result of a categorical variable in relation to the predictor variables [18]. It is an efficient tool for burned area mapping since it offers the chance to obtain the probability of a pixel to be classified as burned or unburned [9,26]. LR provides a good probabilistic framework for the development of burned area algorithms since the models obtained are consistent with variations in environmental variables [21].

2.5. Support Vector Machine

Support vector machine (SVM) is a statistical learning algorithm, robust to data noise and adapted to classification and nonlinear regression problems [10]. SVM transforms a nonlinear regression model into a linear model using kernel functions to map the original input space into a new high-dimensional features space [7]. In this high-dimensional space (hyperplane), SVM finds unique solutions to classification and regression problems [18]. The advantage of SVM over traditional classifiers is that it solves learning problems better when only a small number of training samples are available [27]. SVM has shown good classification results for satellite images, presenting low omission errors [19].

3. Materials and Methods

3.1. Hardware and Software Used

Experiments were conducted in a computer with a processor Intel(R) Core(TM) i7-8565U CPU @1.80GHz 2.00GHz, with 16 GB RAM memory DDR4-2400. As regards the software used, the computer had Ubuntu 18 operating system installed. Codes were programmed with Python 3.6 with numpy, pandas, gdal, networkx, tensorflow and pylab libraries. In addition, Qgis 3 [28] and Google Earth (<https://www.google.com/earth/versions/>, accessed on 30 October 2021) were used to visualize images and to generate the training datasets.

3.2. Study area

The study area corresponds to the territory that extends from the O'Higgins regions to Bío-Bío (33.8°–38.4° S) in Chile (Figure 1). This area has a long history of wildfire occurrence [29], explained by climatic conditions, economic activities and population concentration [30]. Said area presents a semiarid Mediterranean climate, with most rainfalls occurring during the winter period, reaching 350–1300 mm per year, causing a long dry season with low relative humidity, high temperatures and very low precipitations [31]. Since 2010, due to global climatic change, this area has been suffering a prolonged and severe mega drought [32]. The area's natural vegetation is dominated by Mediterranean shrublands and sclerophyllous forests [33]. Moreover, it presents a high presence of land cover areas created by human action, including forest plantations, agricultural farms and wildland-urban interfaces, where human activities make them likely to suffer from wildfires. The period chosen for this study is the 2016–2017 season, during which the phenomenon of mega wildfires in Chile took place. Their magnitudes and intensities forced the creation of an additional level in the scale of measurement used for the classification of wildfires [34]. The damages recorded affected 596 thousand hectares among O'Higgins

and Bío-Bío. The fire destroyed forests, plantations, agricultural farms, meadows and other vegetation masses, affecting more than 2500 homes [35].

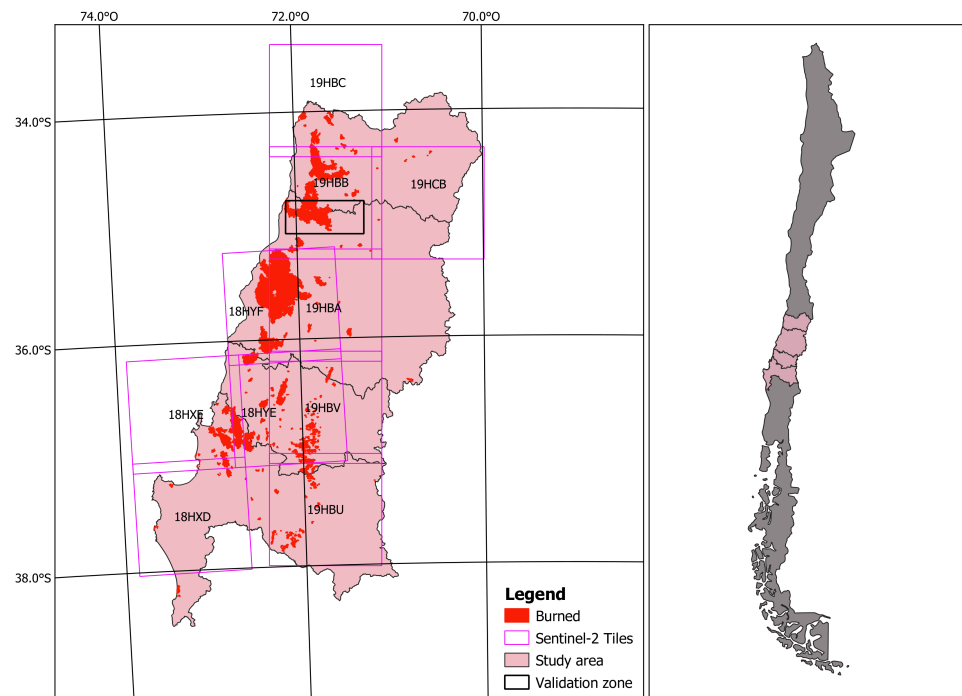


Figure 1. Study area.

3.3. Training Data Extraction and Validation

In order to create the training datasets for the classification algorithms, 20 Sentinel-2 MSI images [36] with cloud cover lower than 30% were considered before and after the fires of the summer of 2017, which mainly occurred between 30 January and 14 February (Table 1). The MSI sensor has 13 spectral bands with frequencies spanning from the Visible and Near-Infrared (VNIR) to the short-wave infrared (SWIR). It has a spatial resolution of 10 m, 20 m and 60 m and 5 days temporal resolution [37]. Data were downloaded from Copernicus open-access hub platform (<https://scihub.copernicus.eu/>, accessed on 18 August 2021) and atmospherically and topographically corrected to obtain surface reflectance (20 m, L2A level) using Sen2cor algorithm [38].

The creation of the dataset was developed by a human expert using false color composite over Sentinel-2 images (Figure 2A), photo interpretation criteria and spectrum analysis to distinguish between burned and unburned areas (Figure 2B).

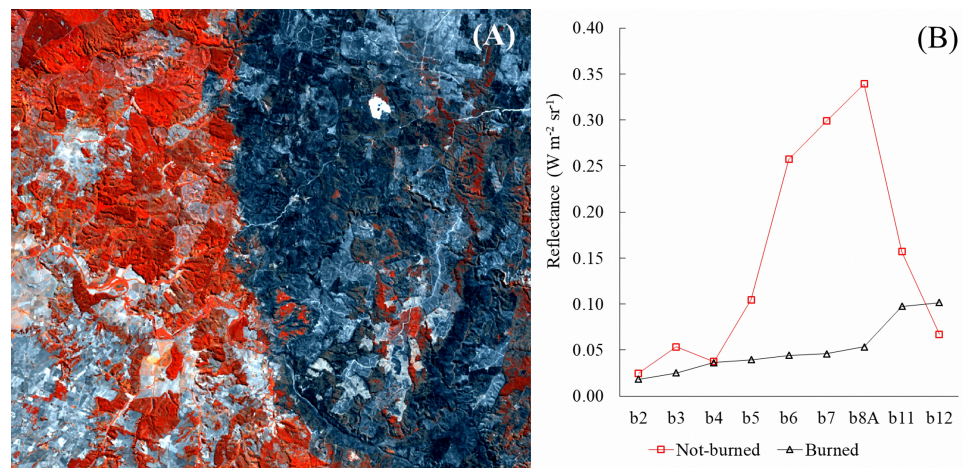


Figure 2. Infrared false-color composite, red and black tones, show unburned and burned vegetation, respectively (A). Spectral signature of unburned and burned vegetation (B).

Table 1. Sentinel-2 images ID Tiles, cover region, date and time of sensing.

Sentinel-2 Tiling Grid ID	Cover Region	Date	Time
19HBC	O'Higgins	19 January 2017	14:37:31 UTC
19HBC	O'Higgins	18 February 2017	14:37:51 UTC
19HBB	O'Higgins	19 January 2017	14:37:31 UTC
19HBB	O'Higgins	18 February 2017	14:37:51 UTC
19HCB	O'Higgins	19 January 2017	14:37:31 UTC
19HCB	O'Higgins	15 February 2017	14:28:51 UTC
18HYF	Maule	19 January 2017	14:37:31 UTC
18HYF	Maule	18 February 2017	14:37:51 UTC
19HBA	Maule	19 January 2017	14:37:31 UTC
19HBA	Maule	28 February 2017	14:37:51 UTC
18HYE	Ñuble	19 January 2017	14:37:31 UTC
18HYE	Ñuble	18 February 2017	14:37:51 UTC
19HBV	Ñuble	6 January 2017	14:27:41 UTC
19HBV	Ñuble	15 February 2017	14:28:51 UTC
18HXE	Bío-Bío	2 January 2017	14:47:22 UTC
18HXE	Bío-Bío	21 February 2017	14:47:31 UTC
18HXD	Bío-Bío	2 January 2017	14:47:22 UTC
18HXD	Bío-Bío	21 February 2017	14:47:31 UTC
19HBU	Bío-Bío	6 January 2017	14:27:41 UTC
19HBU	Bío-Bío	15 February 2017	14:28:51 UTC

Based on the image analysis, two datasets were created:

- POST: pixels values from a post-fire image.
- DELTA: pixels values composed by the difference between a pre-fire and a post-fire image.

For the POST dataset, 100 burned and unburned polygons were built, representing 5.98% of the study area. In the other case, for the DELTA dataset, 80 burned and unburned polygons were selected, adding up to near 2.30% of the study area. In order to ensure the consistency of the datasets, the training polygons were overlapped with several spectral indices that have shown the best response in burned area detection [39,40] (Table 2).

Table 2. Spectral indices used for burned area identification.

Index	Formulation
BAI [41]	$\frac{1}{(0.1 - b4)^2 + (0.06 - b8A)^2}$
BAIS2 [5]	$\left(1 - \sqrt{\frac{b6 \cdot b7 \cdot b8A}{b4}}\right) \cdot \left(\frac{b12 - b8A}{\sqrt{b12 + b8A}} + 1\right)$
MIRBI [42]	$(10 \cdot b12 - 9.8 \cdot b11 + 2)$
NBR2 [43]	$\frac{(b11 - b12)}{(b11 + b12)}$

where: $b4$: Reflectance in the red band (centered at 0.665 μm). $b6$: Reflectance in the near-infrared band 1 (centered at 0.665 μm). $b8A$: Reflectance in the near-infrared band 2 (centered at 0.865 μm). $b11$: Reflectance in the shortwave infrared band 1 (centered at 1.610 μm). $b12$: Reflectance in the shortwave infrared band 1 (centered at 2.190 μm).

3.4. Analysis and Filtering of Training Datasets

One of the main steps to achieve a successfully supervised classification is to have a good training dataset [44]. For that, we analyzed the POST and DELTA datasets in order to remove those pixels that could eventually be misclassified by the expert or showed low separability values. We evaluated the mean; median; standard deviation; 1, 2 and 3 quartiles; and minimum and maximum values for the burned and unburned categories, and eliminated the atypical found values. Regarding separability, several indexes or distances can be applied to image classification [45]. However, for burned-area classification, the separability index (SI) [46] (equation (5)) has been broadly used on different sensors and ecosystems [5,9,47] to select spectral bands and indices that provide a higher discriminating capacity ($SI \geq 0.75$) to the classification process.

$$SI = \frac{|\mu_q - \mu_{nq}|}{\delta_q + \delta_{nq}} \quad (5)$$

where:

μ_q : mean of the burned category.

μ_{nq} : mean of the unburned category.

δ_q : standard deviation of the burned category.

δ_{nq} : standard deviation of the unburned category.

Training datasets were randomly balanced in order to obtain the same number of pixels for the burned and unburned categories. This allows for the the proper training of the supervised classifiers [22].

3.5. Experiments

The original set was randomly divided into three sets with the following percentages of the total amount of data: 50% for the training set, 20% for the validation set and 30% for the test set. The training set is used to calculate the classifiers parameters, the validation set offers the chance to choose the best model among those generated by the combination of hyperparameters and the test set is used to carry out the objective performance evaluation of each classification algorithm. The following variations to the hyperparameters of the classification algorithms were conducted:

- ELM: the best model was selected among ELM networks with 1, 2, 3, 4, ..., 498, 499 and 500 neurons in the hidden layer.
- Random forest: training and tests were conducted with 5, 10, 15, 20, ..., 985, 990, 995 and 1000 random trees.
- Logistic regression: training and tests were conducted with 5, 10, 15, 20, ..., 985, 990, 995 and 1000 as the maximum number of iterations for convergence.

- Support vector machine: a polynomial core was used that shows a better performance than radial basis kernel [48] and that has been widely applied in this type of classification [49].
- Multilayer perceptron: training and tests were carried out with a single hidden layer multilayer perceptron, from 1 to 100 neurons, with rectified linear unit activation function (relu) and using the Adam stochastic optimizer [50].

In order to choose the best model among the variations generated by the hyperparameters, the average of global accuracy and the DICE coefficients [9] was calculated over the validation set (Figure 3).

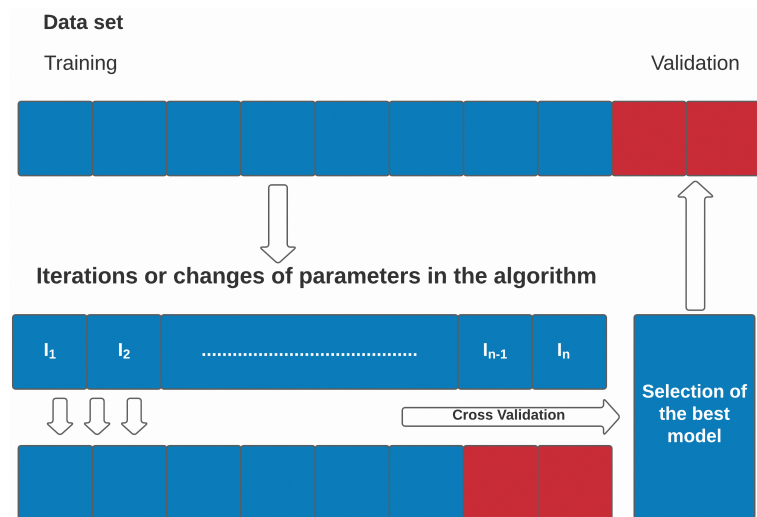


Figure 3. Training and validation strategy.

According to Padilla et al. [51], obtaining an accurate analysis of burned classifications or products is much more relevant to consider the accuracy of the “burned” category than the “unburned” because the first is more related to the impacts of biomass burning and its atmospheric effects. For that, the performance of the best models for the burned category was evaluated in the test set with DICE coefficient, omission and commission errors, which have been used in several studies that compared accuracies for burned area classifications [9,13,52]. The DICE coefficient measures accuracy with a probabilistic meaning [40], and the accuracy, omission and commission errors are getting from the confusion matrix [53]. In addition, we evaluated the models according to their training time [14]. Finally, the performance of the selected model was compared using an independent validation area. The validation area was built from a supervised classification of Sentinel-2 (20 m) images from a section of 247,401 hectares from the Maule Region, representing 2.96% of the study area. The classification performance of the best model was compared to the estimations of burned area done by the Chile’s National Forest Corporation (CONAF) (<https://sit.conaf.cl/>, accessed on 23 September 2021) and the FireCCI product [54].

4. Results and Discussion

4.1. Separability of Indices and Bands

Figure 4 shows that the highest values for the SI index occur mainly for the DELTA dataset. This demonstrates the advantage of using a multitemporal strategy to improve discrimination of the categories that have suffered spectral changes due to wildfires [9,55]. Furthermore, it is observed that for the DELTA dataset, the higher values are obtained by the spectral indices and not by individual bands. This shows the higher sensitivity of spectral indices that are designed to enhance the signal of burned areas [56]. As regards individual bands, those within the NIR zone (b6, b7 and b8A) show high separability values, which occur due to the great difference between the reflectance of vegetation affected or not

affected by fire [4,57]. The NIR area is particularly sensitive to the internal cellular structure of leaves, and it reflects changes when an alteration takes place in this structure due to fire, senescence, a pathogen or deficiency of macronutrients [39]. On the contrary, bands of the visible zone (b2, b3, b4) show poor discrimination power, concurrent with what was obtained in [56]. Given the discrimination criteria considered, the features selected for training were the b6, b7 and b8A bands, and all of the spectral indices.

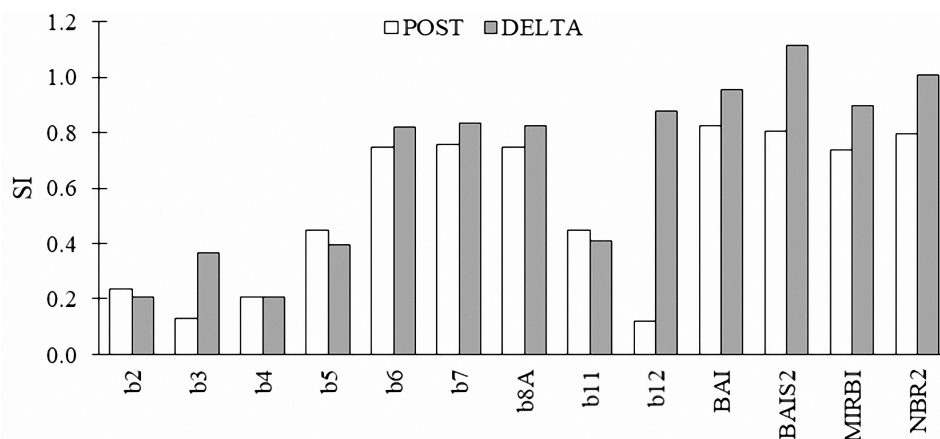


Figure 4. Separability of classes in bands and indices for POST and DELTA datasets.

4.2. Performance Statistics

4.2.1. POST Dataset

Table 3 presents the performance of the best model obtained from the POST dataset for the validation set. On the other hand, Table 4 shows the best model performance of POST data for the test set. The highest performance in both tables was obtained by RF, followed by ELM, SVM, LR and MLP. As was expected, the test set experienced a low decrease in DICE and accuracy performance indicators, but an improvement for omission and commission errors.

Table 3. Best model performance for the POST dataset applied over the validation set.

Algorithm	DICE	Accuracy	Omission	Commission
RF	0.92	0.93	0.08	0.09
SVM	0.87	0.88	0.16	0.09
LR	0.88	0.89	0.14	0.11
MLP	0.87	0.87	0.10	0.14
ELM	0.92	0.92	0.02	0.12

where RF: random forest; SVM: support vector machine; LR: logistic regression; MLP: multilayer perceptron; and ELM: extreme learning machine.

Table 4. Best model performance for the POST dataset applied over the Test set.

Algorithm	DICE	Accuracy	Omission	Commission
RF	0.93	0.92	0.08	0.08
SVM	0.86	0.88	0.12	0.10
LR	0.88	0.88	0.12	0.10
MLP	0.80	0.85	0.01	0.12
ELM	0.89	0.89	0.01	0.11

4.2.2. DELTA Dataset

Table 5 presents the best model performance for the validation set and Table 6 the best model performance for the test set. It is observed that the classifiers have better performance for the DELTA dataset than for the POST dataset, seemingly due to the fact that DELTA

shows higher levels of SI in almost all the features analyzed (Figure 4). Moreover, the order of performance of the algorithms is maintained for the POST dataset, showing a similar decreasing tendency for the test dataset indicators.

Table 5. Best model performance over the DELTA dataset for the validation set.

Algorithm	DICE	Accuracy	Omission	Commission
RF	0.94	0.94	0.08	0.06
SVM	0.89	0.89	0.16	0.08
LR	0.84	0.84	0.11	0.16
MLP	0.89	0.89	0.04	0.12
ELM	0.93	0.92	0.12	0.02

Table 6. Best model performance over the DELTA dataset for the test set.

Algorithm	DICE	Accuracy	Omission	Commission
RF	0.92	0.93	0.07	0.08
SVM	0.87	0.89	0.16	0.08
LR	0.84	0.83	0.17	0.19
MLP	0.86	0.85	0.10	0.10
ELM	0.91	0.91	0.12	0.02

In [7], similar results were obtained when RF was compared to SVM and MLP over MODIS data with 500 m resolution. In this study, the worst performance for most algorithms occurred for the POST dataset. This may have been caused by the high variability of the burned class [58]. On the contrary, this variability was considerably reduced for the DELTA dataset, which accounts for the better performance of the algorithms [52]. The problems mentioned in the POST dataset could be reduced, including a larger amount of training samples of different land covers and burned zones with different conditions [59]. Although the data used for the training sets were thoroughly revised, a high number of pixels with atypical values were found, which could have been wrongly classified. This highlights the importance of adopting a strategy of several steps where the results obtained are refined through the elimination or inclusion of training areas in the most conflicting zones [59].

Mostly, omission errors had a greater magnitude over the DELTA sets than over the POST sets. The opposite took place for commission errors. Omissions can be explained by the high variability of burned areas, which present zones of different levels of severity and cover, such as shrublands and agricultural burning. Some of them present both low contrast with their unburned environment and areas in which vegetation has begun recovering after the fire [9]. On the other hand, commission errors were caused by the topographic shading that was not completely removed by the correction conducted, the presence of elements of great height (trees that cast shadows on border areas) [59], areas with scarce vegetation and high presence of soil (agricultural and forest harvested), whose spectral changes are consistent with burned areas [60].

4.3. Time Statistics

Figure 5 shows the training time of the best model of the classifiers used for both POST and DELTA datasets. ELM (1.45 s) and LR (1.85 s) algorithms recorded the shortest training times, followed by SVM (6.2 s) and RF (35.1 s). In line with the hypothesis, ELM neural network training times are shorter than the rest of the classifiers. This is due to the fact that the training algorithm does not optimize all the network parameters and the calculation of the Moore–Penrose pseudoinverse is highly efficient [61].

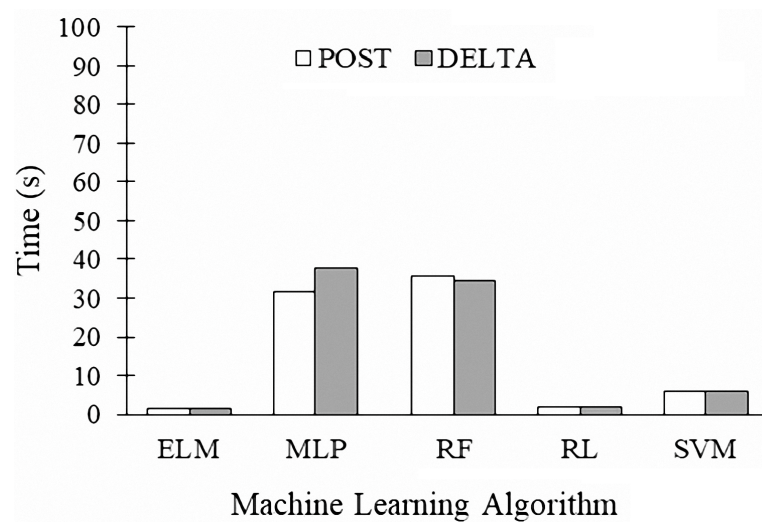


Figure 5. Training time for classification algorithms applied to POST and DELTA datasets.

4.4. Comparison of the ELM Classification with Burned Area Products

This section presents a comparison with methods of estimation of burned areas operatively used, namely, the method used by CONAF [62] and the FireCCI algorithm [54].

The best indicators in the validation area were reached by ELM, followed by CONAF and FIRECCI (Table 7). The higher spatial coincidence (DICE = 0.857) occurred between the classification carried out by ELM and the reference one, resulting in low omission (0.080) and commission (0.132) errors. The spatial coincidence of ELM classification with the reference data is observed in the detailed description that the ELM carries out over the burned-area borders and in the capacity to describe the internal islands that were not affected by fire (Figure 6D). This was explained by the proper training of the network, its generalization capacity, and the correspondence with the spatial resolution of the images used. On the other hand, estimates by CONAF showed lower spatial coincidence with respect to the classification of reference, having a DICE of 0.799, with omission and commission errors of 0.064 and 0.301, respectively. Despite showing a good spatial coincidence with its reference, and using Landsat 7 and 8 images [62], the estimate by CONAF showed a higher number of commission errors. They can be presumably caused by a general visual interpretation of the areas affected by fire, making it hard to account for the complexity of the geometry of the burned polygons and the unburned islands (Figure 6B). Moreover, FIRECCI estimations showed the worst results for the validation metrics. The low spatial resolution of the FIRECCI product (250 m) prevents it from detecting internal unburned islands, which are located to the interior of the big burned patches (Figure 6C). Furthermore, it prevents it from detecting low-intensity fires, mainly of agricultural origin [13].

Table 7. ELM–CONAF–FIRECCI comparison.

-	Ground Truth	ELM	CONAF	FIRECCI
Burned area (ha)	37,472.28	39,702.96	50,216.84	43,868.44
Unburned area (ha)	209,928.72	207,698.04	197,184.16	203,532.56
DICE	1	0.857	0.799	0.773
Omission	0	0.080	0.064	0.160
Commission	0	0.132	0.301	0.282

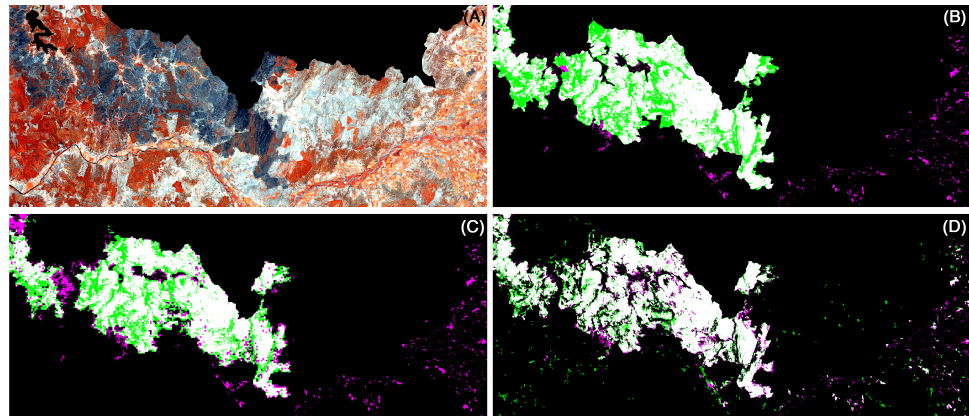


Figure 6. Burned area classifications for the validation area (A), CONAF's Method (B), FIRECCI Algorithm (C) and ELM (D). White shows spatial agreement, and magenta indicates omission and green shows commission.

5. Conclusions

This study has evaluated the potential of ELM neural networks as a new burned area classifier of multispectral Sentinel-2 satellite images. ELM showed promising results in the classification performance on the test dataset and shorter training times than the other algorithms. This characteristic is a great advantage for ELM in order to address burned area mapping with medium-high spatial resolution images at national and global scales. However, like the other machine-learning algorithms, its practical implementation requires preprocessing stages that include an atmospheric and topographic correction and samples collection to generate training datasets with enough spectral and spatial representativity of the burned areas.

In the current context of climate change, where an increase in the frequency and magnitude of wildfires is forecasted, there is a growing need for precise information about burned areas. This information is essential to fire risk systems and burned-area records used to design prevention and fire-combat strategies and provides valuable knowledge on the effect of fires on the landscape and the atmosphere.

Author Contributions: Conceptualization, J.G. and M.M.; methodology, J.G. and M.M.; software, G.V.-N.; validation, J.G., M.M. and G.V.-N.; formal analysis, J.G., M.M. and M.C.-B.; investigation, J.G., M.M. and G.V.-N.; resources, J.G. and M.M.; data curation, J.G. and G.V.-N.; writing—original draft preparation, J.G., M.M., M.C.-B. and G.V.-N.; supervision, J.G. and M.M.; project administration, J.G.; funding acquisition, J.G. and M.M. All authors have read and agreed to the published version of the manuscript.

Funding: This research was partially funded by the Fondo de Investigación del Bosque Nativo (FIBN) from Corporación Nacional Forestal de Chile (CONAF), grant number FIBN010/2017.

Acknowledgments: The authors of this study offer their special thanks to the FONDECYT Regular Project 2020 No. 1200810 “Very Large Fingerprint Classification based on a Fast and Distributed Extreme Learning Machine”, National Agency of Investigation and Development, Science, Technology, Knowledge and Innovation Ministry, Government of Chile, from where the methodology of work of ELM networks was obtained.

Conflicts of Interest: The authors declare no conflict of interest. The funders had no role in the design of the study; in the collection, analyses, or interpretation of data; in the writing of the manuscript; or in the decision to publish the results.

Abbreviations

The following abbreviations are used in this manuscript:

RF	random forest
SVM	support vector machine
LR	logistic regression
MLP	multilayer perceptron
ELM	extreme learning machine
NIR	near-infrared
VNIR	Visible- and Near-Infrared
SWIR	short-wave infrared
NBR	normalized burn ratio
NDVI	normalized difference vegetation index
SI	separability index

References

- Salinero, E.C. Detección y análisis de incendios forestales desde satélites de teledetección. *Rev. Real Acad. Cienc. Exactas Físicas Nat.* **2009**, *103*, 173–182.
- Liu, Y.; Stanturf, J.; Goodrick, S. Trends in global wildfire potential in a changing climate. *For. Ecol. Manag.* **2010**, *259*, 685–697. [[CrossRef](#)]
- Knopp, L.; Wieland, M.; Rättich, M.; Martinis, S. A deep learning approach for burned area segmentation with Sentinel-2 data. *Remote Sens.* **2020**, *12*, 2422. [[CrossRef](#)]
- Pereira, J.M.; Govaerts, Y. Potential fire applications from MSG/SEVIRI observations. Technical Memorandum No 7. *Darmstadt Eumetsat* **2001**, *41*.
- Filipponi, F. BAI52: Burned area index for Sentinel-2. *Multidiscip. Digit. Publ. Inst. Proc.* **2018**, *2*, 364. [[CrossRef](#)]
- Anaya, J.; Sione, W.; Rodríguez-Montellano, A. Identificación de áreas quemadas mediante el análisis de series de tiempo en el ámbito de computación en la nube. *Rev. Teledetección* **2018**, *51*, 61–73. [[CrossRef](#)]
- Ramo, R.; García, M.; Rodríguez, D.; Chuvieco, E. A data mining approach for global burned area mapping. *Int. J. Appl. Earth Obs. Geoinf.* **2018**, *73*, 39–51. [[CrossRef](#)]
- Jain, P.; Coogan, S.C.; Subramanian, S.G.; Crowley, M.; Taylor, S.; Flannigan, M.D. A review of machine learning applications in wildfire science and management. *Environ. Rev.* **2020**, *28*, 478–505. [[CrossRef](#)]
- Roteta, E.; Bastarrika, A.; Padilla, M.; Storm, T.; Chuvieco, E. Development of a Sentinel-2 burned area algorithm: Generation of a small fire database for sub-Saharan Africa. *Remote Sens. Environ.* **2019**, *222*, 1–17. [[CrossRef](#)]
- Petropoulos, G.P.; Kontoes, C.; Keramitsoglou, I. Burnt area delineation from a uni-temporal perspective based on Landsat TM imagery classification using Support Vector Machines. *Int. J. Appl. Earth Obs. Geoinf.* **2011**, *13*, 70–80. [[CrossRef](#)]
- Pu, R.; Gong, P. Determination of burnt scars using logistic regression and neural network techniques from a single post-fire Landsat 7 ETM+ image. *Photogramm. Eng. Remote Sens.* **2004**, *70*, 841–850. [[CrossRef](#)]
- Ba, R.; Song, W.; Li, X.; Xie, Z.; Lo, S. Integration of multiple spectral indices and a neural network for burned area mapping based on MODIS data. *Remote Sens.* **2019**, *11*, 326. [[CrossRef](#)]
- Ramo, R.; Roteta, E.; Bistinas, I.; Van Wees, D.; Bastarrika, A.; Chuvieco, E.; Van der Werf, G.R. African burned area and fire carbon emissions are strongly impacted by small fires undetected by coarse resolution satellite data. *Proc. Natl. Acad. Sci. USA* **2021**, *118*, e2011160118. [[CrossRef](#)]
- Osisanwo, F.; Akinsola, J.; Awodele, O.; Hinmikaiye, J.; Olakanmi, O.; Akinjobi, J. Supervised machine-learning algorithms: classification and comparison. *Int. J. Comput. Trends Technol.* **2017**, *48*, 128–138.
- Huang, G.; Huang, G.B.; Song, S.; You, K. Trends in extreme learning machines: A review. *Neural Netw.* **2015**, *61*, 32–48. [[CrossRef](#)] [[PubMed](#)]
- Huang, G.B.; Zhu, Q.Y.; Siew, C.K. Extreme learning machine: A new learning scheme of feedforward neural networks. In *Proceedings of the 2004 IEEE International Joint Conference on Neural Networks (IEEE Cat. No. 04CH37541)*, Budapest, Hungary, 25–29 July 2004; Volume 2, pp. 985–990.
- Peterson, K.T.; Sagan, V.; Sidike, P.; Cox, A.L.; Martinez, M. Suspended sediment concentration estimation from landsat imagery along the lower missouri and middle Mississippi Rivers using an extreme learning machine. *Remote Sens.* **2018**, *10*, 1503. [[CrossRef](#)]
- Hultquist, C.; Chen, G.; Zhao, K. A comparison of Gaussian process regression, random forests and support vector regression for burn severity assessment in diseased forests. *Remote Sens. Lett.* **2014**, *5*, 723–732. [[CrossRef](#)]
- Mallinis, G.; Koutsias, N. Comparing ten classification methods for burned area mapping in a Mediterranean environment using Landsat TM satellite data. *Int. J. Remote Sens.* **2012**, *33*, 4408–4433. [[CrossRef](#)]
- Schowengerdt, R.A. *Remote Sensing: Models and Methods for Image Processing*; Elsevier: Amsterdam, The Netherlands, 2006.
- De Vasconcelos, M.P.; Silva, S.; Tome, M.; Alvim, M.; Pereira, J.C. Spatial prediction of fire ignition probabilities: Comparing logistic regression and neural networks. *Photogramm. Eng. Remote Sens.* **2001**, *67*, 73–81.

22. Ramo, R.; Chuvieco, E. Developing a random forest algorithm for MODIS global burned area classification. *Remote Sens.* **2017**, *9*, 1193. [[CrossRef](#)]
23. Belgiu, M.; Drăguț, L. Random forest in remote sensing: A review of applications and future directions. *ISPRS J. Photogramm. Remote Sens.* **2016**, *114*, 24–31. [[CrossRef](#)]
24. Gislason, P.O.; Benediktsson, J.A.; Sveinsson, J.R. Random forests for land cover classification. *Pattern Recognit. Lett.* **2006**, *27*, 294–300. [[CrossRef](#)]
25. Collins, L.; Griffioen, P.; Newell, G.; Mellor, A. The utility of Random Forests for wildfire severity mapping. *Remote Sens. Environ.* **2018**, *216*, 374–384. [[CrossRef](#)]
26. Fraser, R.H.; Fernandes, R.; Latifovic, R. Multi-temporal burned area mapping using logistic regression analysis and change metrics. In Proceedings of the IEEE International Geoscience and Remote Sensing Symposium, Toronto, ON, Canada, 24–28 June 2002; Volume 3, pp. 1486–1488.
27. Cao, X.; Chen, J.; Matsushita, B.; Imura, H.; Wang, L. An automatic method for burn scar mapping using support vector machines. *Int. J. Remote Sens.* **2009**, *30*, 577–594. [[CrossRef](#)]
28. QGIS Development Team. *QGIS Geographic Information System*; QGIS Association: Beaverton, OR, USA, 2018.
29. González, M.E.; Gómez-González, S.; Lara, A.; Garreaud, R.; Díaz-Hormazábal, I. The 2010–2015 Megadrought and its influence on the fire regime in central and south-central Chile. *Ecosphere* **2018**, *9*, e02300. [[CrossRef](#)]
30. Sarricolea, P.; Serrano-Notivol, R.; Fuentealba, M.; Hernández-Mora, M.; De la Barrera, F.; Smith, P.; Meseguer-Ruiz, Ó. Recent wildfires in Central Chile: Detecting links between burned areas and population exposure in the wildland urban interface. *Sci. Total. Environ.* **2020**, *706*, 135894. [[CrossRef](#)]
31. Gómez-González, S.; González, M.E.; Paula, S.; Díaz-Hormazábal, I.; Lara, A.; Delgado-Baquerizo, M. Temperature and agriculture are largely associated with fire activity in Central Chile across different temporal periods. *For. Ecol. Manag.* **2019**, *433*, 535–543. [[CrossRef](#)]
32. Garreaud, R.D.; Boisier, J.P.; Rondanelli, R.; Montecinos, A.; Sepúlveda, H.H.; Veloso-Aguila, D. The Central Chile Mega Drought (2010–2018): A climate dynamics perspective. *Int. J. Climatol.* **2020**, *40*, 421–439. [[CrossRef](#)]
33. McWethy, D.B.; Pauchard, A.; García, R.A.; Holz, A.; González, M.E.; Veblen, T.T.; Stahl, J.; Currey, B. Landscape drivers of recent fire activity (2001–2017) in south-central Chile. *PLoS ONE* **2018**, *13*, e0201195. [[CrossRef](#)]
34. De la Barrera, F.; Barraza, F.; Favier, P.; Ruiz, V.; Quense, J. Megafires in Chile 2017: Monitoring multiscale environmental impacts of burned ecosystems. *Sci. Total. Environ.* **2018**, *637*, 1526–1536. [[CrossRef](#)]
35. CONAF. Análisis de la Afectación y Severidad de los Incendios Forestales Ocurredos en Enero y Febrero de 2017 Sobre los usos de Suelo y los Ecosistemas Naturales Presentes entre las Regiones de COQUIMBO y Los Ríos de Chile. Available online: https://www.conaf.cl/tormenta_de_fuego-2017/INFORME-AFECTACION-Y_SEVERIDAD-DE-INCENDIOS-FORESTALES-VERANO-2017-SOBRE-ECOSISTEMAS-VEGETACIONALES-CONAF.pdf (accessed on 1 November 2021).
36. Drusch, M.; Del Bello, U.; Carlier, S.; Colin, O.; Fernandez, V.; Gascon, F.; Hoersch, B.; Isola, C.; Laberinti, P.; Martimort, P.; et al. Sentinel-2: ESA's optical high-resolution mission for GMES operational services. *Remote Sens. Environ.* **2012**, *120*, 25–36. [[CrossRef](#)]
37. Gatti, A.; Bertolini, A. Sentinel-2 Products Specification Document. 2013. Available online: <https://earth.esa.int/documents/247904/685211/Sentinel-2+Products+Specification+Document> (accessed on 23 February 2015).
38. Louis, J.; Debaecker, V.; Pflug, B.; Main-Knorn, M.; Bieniarz, J.; Mueller-Wilm, U.; Cadau, E.; Gascon, F. Sentinel-2 Sen2Cor: L2A processor for users. In *Proceedings Living Planet Symposium 2016*; Spacebooks: Online, 2016; pp. 1–8.
39. Fornacca, D.; Ren, G.; Xiao, W. Evaluating the best spectral indices for the detection of burn scars at several post-fire dates in a mountainous region of Northwest Yunnan, China. *Remote Sens.* **2018**, *10*, 1196. [[CrossRef](#)]
40. Fleiss, J.L.; Levin, B.; Paik, M.C. *Statistical Methods for Rates and Proportions*; John Wiley & Sons: Hoboken, NJ, USA, 2013.
41. Martín, M.P.; Chuvieco, E. Cartografía de grandes incendios forestales en la Península Ibérica a partir de imágenes NOAA-AVHRR. *Ser. Geográfica* **1998**, *7*, 109–128.
42. Trigg, S.; Flasse, S. An evaluation of different bi-spectral spaces for discriminating burned shrub-savannah. *Int. J. Remote Sens.* **2001**, *22*, 2641–2647. [[CrossRef](#)]
43. García, M.L.; Caselles, V. Mapping burns and natural reforestation using Thematic Mapper data. *Geocarto Int.* **1991**, *6*, 31–37. [[CrossRef](#)]
44. Mohajane, M.; Essahlaoui, A.; Oudija, F.; Hafyani, M.E.; Hmaid, A.E.; Ouali, A.E.; Randazzo, G.; Teodoro, A.C. Land use/land cover (LULC) using landsat data series (MSS, TM, ETM+ and OLI) in Azrou Forest, in the Central Middle Atlas of Morocco. *Environments* **2018**, *5*, 131. [[CrossRef](#)]
45. Randazzo, G.; Cascio, M.; Fontana, M.; Gregorio, F.; Lanza, S.; Muzirafuti, A. Mapping of Sicilian Pocket Beaches Land Use/Land Cover with Sentinel-2 Imagery: A Case Study of Messina Province. *Land* **2021**, *10*, 678. [[CrossRef](#)]
46. Kaufman, Y.J.; Remer, L.A. Detection of forests using mid-IR reflectance: an application for aerosol studies. *IEEE Trans. Geosci. Remote Sens.* **1994**, *32*, 672–683. [[CrossRef](#)]
47. Liu, S.; Zheng, Y.; Dalponte, M.; Tong, X. A novel fire index-based burned area change detection approach using Landsat-8 OLI data. *Eur. J. Remote Sens.* **2020**, *53*, 104–112. [[CrossRef](#)]
48. Kerdprasop, N.; Poomka, P.; Chuaybamroong, P.; Kerdprasop, K. Forest Fire Area Estimation using Support Vector Machine as an Approximator. *IJCCI* **2018**, 269–273.

49. Bar, S.; Parida, B.R.; Pandey, A.C. Landsat-8 and Sentinel-2 based Forest fire burn area mapping using machine-learning algorithms on GEE cloud platform over Uttarakhand, Western Himalaya. *Remote Sens. Appl. Soc. Environ.* **2020**, *18*, 100324.
50. Kingma, D.P.; Ba, J. Adam: A method for stochastic optimization. *arXiv* **2014**, arXiv:1412.6980.
51. Padilla, M.; Stehman, S.V.; Chuvieco, E. Validation of the 2008 MODIS-MCD45 global burned area product using stratified random sampling. *Remote Sens. Environ.* **2014**, *144*, 187–196. [[CrossRef](#)]
52. Roteta, E.; Bastarrika, A.; Franquesa, M.; Chuvieco, E. Landsat and Sentinel-2 Based Burned Area Mapping Tools in Google Earth Engine. *Remote Sens.* **2021**, *13*, 816. [[CrossRef](#)]
53. Congalton, R.G.; Green, K. *Assessing the Accuracy of Remotely Sensed Data: Principles and Practices*; CRC Press: Boca Raton, FL, USA, 2019.
54. Chuvieco, E.; Lizundia-Loiola, J.; Pettinari, M.L.; Ramo, R.; Padilla, M.; Tansey, K.; Mouillot, F.; Laurent, P.; Storm, T.; Heil, A.; et al. Generation and analysis of a new global burned area product based on MODIS 250 m reflectance bands and thermal anomalies. *Earth Syst. Sci. Data* **2018**, *10*, 2015–2031. [[CrossRef](#)]
55. Bastarrika, A.; Chuvieco, E.; Martín, M.P. Mapping burned areas from Landsat TM/ETM+ data with a two-phase algorithm: Balancing omission and commission errors. *Remote Sens. Environ.* **2011**, *115*, 1003–1012. [[CrossRef](#)]
56. Huang, H.; Roy, D.P.; Boschetti, L.; Zhang, H.K.; Yan, L.; Kumar, S.S.; Gomez-Dans, J.; Li, J. Separability analysis of Sentinel-2A multi-spectral instrument (MSI) data for burned area discrimination. *Remote Sens.* **2016**, *8*, 873. [[CrossRef](#)]
57. Roy, D.P.; Jin, Y.; Lewis, P.; Justice, C. Prototyping a global algorithm for systematic fire-affected area mapping using MODIS time series data. *Remote Sens. Environ.* **2005**, *97*, 137–162. [[CrossRef](#)]
58. Bastarrika, A.; Alvarado, M.; Artano, K.; Martinez, M.P.; Mesanza, A.; Torre, L.; Ramo, R.; Chuvieco, E. BAMS: A tool for supervised burned area mapping using Landsat data. *Remote Sens.* **2014**, *6*, 12360–12380. [[CrossRef](#)]
59. Roteta, E.; Oliva, P. Optimization Of A Random Forest Classifier For Burned Area Detection In Chile Using Sentinel-2 Data. In Proceedings of the 2020 IEEE Latin American GRSS & ISPRS Remote Sensing Conference (LAGIRS), Santiago, Chile, 22–26 March 2020; pp. 568–573.
60. Korontzi, S.; McCarty, J.; Loboda, T.; Kumar, S.; Justice, C. Global distribution of agricultural fires in croplands from 3 years of Moderate Resolution Imaging Spectroradiometer (MODIS) data. *Glob. Biogeochem. Cycles* **2006**, *20*. [[CrossRef](#)]
61. Huang, G.B.; Zhou, H.; Ding, X.; Zhang, R. Extreme learning machine for regression and multiclass classification. *IEEE Trans. Syst. Man Cybern. Part B* **2011**, *42*, 513–529. [[CrossRef](#)] [[PubMed](#)]
62. CONAF. *Uso del Suelo Afectado por Incendios Forestales Sobre 200 Hectareas entre 1 de Enero y 10 de Febrero, Desde las Regiones de Coquimbo a la Araucanía—Segunda Actualización*; Technical Report; Corporación Nacional Forestal de Chile: Santiago, Chile, 2017.